

Modeling of efficient dual-junction all-inorganic perovskite tandem cells via SCAPS-1D



Jothika Balasubramaniyan ^a, Thangaraji Vasudevan ^b, Govindaraj Rajamanickam ^a, Lung-Chien Chen ^{b,*}

^a Department of Physics, Sri Sivasubramaniya Nadar College of Engineering, Kalavakkam, Tamil Nadu 603110, India

^b Department of Electro-Optical Engineering, National Taipei University of Technology, Taipei City 10608, Taiwan, ROC

ARTICLE INFO

Keywords:
 Tandem Perovskite solar cells
 $\text{CsPbI}_3/\text{CsSnI}_3$
 CZTS
 HTL-free
 SCAPS-1D
 Simulation and modelling

ABSTRACT

This investigation delivers a detailed SCAPS-1D simulation of all-inorganic, tandem-inspired perovskite solar cells (PSC) utilizing a two-layer absorber configuration. The device configuration $\text{FTO}/\text{TiO}_2/\text{CsPbI}_3/\text{CsSnI}_3$ was evaluated in the presence and absence of a hole transport layer (HTL), using various back contact materials such as gold (Au), silver (Ag), carbon, and CZTS. CsPbI_3 (wide bandgap) functions as the top absorber, while CsSnI_3 (narrow bandgap) serves as the bottom absorber, allowing strong light harvesting over a wide spectral range. A high-power conversion efficiency (PCE) of 33.75% was attained in the HTL-free configuration. Additionally, replacing conventional metal electrodes with cost-effective, sustainable CZTS maintained excellent device performance. These results demonstrate that efficient energy band alignment and charge transport are achievable without organic HTLs, simplifying the device structure while maintaining high efficiency. This work underscores the potential of all-inorganic, tandem-inspired perovskite architectures for scalable, efficient, and eco-friendly photovoltaic technologies.

1. Introduction

Growing energy needs and sustainability goals have driven increased research into alternative technologies that can replace conventional fossil fuels [1]. Among various energy sources, solar energy stands out as a top contender because of its widespread availability and renewable nature [2]. Perovskite solar cells (PSCs) are widely recognized in solar research for their exceptional power conversion gains, simple fabrication processes, and highly tunable optoelectronic properties [3]. Perovskite (PVSK) refers to a specific crystal structure of light-harvesting materials, typically expressed by the formula ABX_3 , ‘A’ represents a monovalent cation, ‘B’ is a divalent metal cation, and ‘X’ denotes a halide anion [4,5]. Since their introduction in 2009, PSCs have achieved a remarkable efficiency increase from 3.8 % to 26.8 %, positioning them as serious contenders to traditional silicon (Si)-based solar cells [6]. Despite the impressive efficiency gains, conventional organic-inorganic hybrid PSCs experience degradation over time, mainly from their susceptibility to moisture, temperature, and ultraviolet light-instabilities often attributed to their organic components [7]. While hybrid PSCs with over 26 % efficiency are now comparable to commercial silicon

photovoltaics, their degradation under ambient conditions hinders large-scale deployment [8,9].

To address these issues, fully inorganic PSCs have been developed as a promising alternative. These cells use inorganic PVSK materials, typically with the formula CsBX_3 , offering enhanced thermal, environmental, and structural stability [10,11]. Materials such as CsPbI_3 , CsPbBr_3 , CsPbIBr_2 , and CsSnI_3 have garnered attention for their favorable optoelectronic properties and improved durability [12–14]. Single-junction solar cells utilize CsPbI_3 because of its compatible bandgap (~ 1.73 eV), though it suffers from phase instability, transitioning from its photoactive phase to a non-photoactive phase in open-air conditions. CsPbBr_3 , while structurally stable and moisture resistant, has a wider bandgap (~ 2.3 eV), limiting its visible-light absorption and efficiency [15,16]. Mixed-halide compositions such as CsPbIBr_2 aim to balance bandgap tunability with improved environmental stability, making them attractive for tandem cell designs [17]. Additionally, CsSnI_3 , a PVSK free of lead with a narrow bandgap of ~ 1.3 eV, addresses environmental toxicity concerns and offers strong near-infrared absorption, making it suitable as a bottom absorber in tandem or bilayer architectures [18,19].

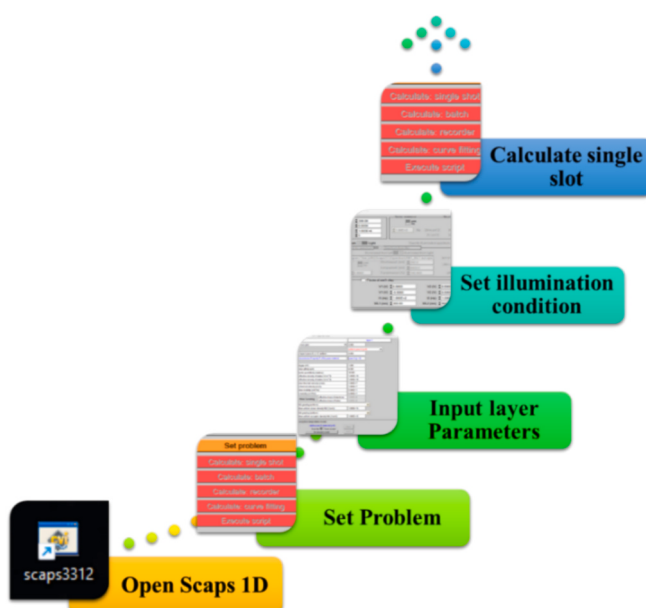
* Corresponding author.

E-mail address: ocean@ntut.edu.tw (L.-C. Chen).

Table 1

Parameters used in simulating each layer of the PSC.

Parameter	FTO	ETL (TiO ₂)	CsPbI ₃	CsSnI ₃	CZTS
thickness (nm)	300	100	200–800	200–800	300
Energy bandgap, Eg (eV)	3.5	3.2	1.7	1.3	1.4
Electron Affinity, χ (eV)	4	4.2	3.95	3.6	4.1
Dielectric permittivity, ϵ_r	9	9	6	9	9
CB effective density of states, NC (1 cm ⁻³)	2×10^{18}	2.1×10^{18}	1.1×10^{20}	1×10^{19}	2.2×10^{18}
VB effective density of states, NV (1 cm ⁻³)	1.8×10^{18}	1×10^{19}	8.2×10^{20}	1×10^{19}	1.8×10^{18}
Electron mobility, μ_n (cm ² /V s)	20	20	25	1.5×10^3	1×10^2
Hole mobility, μ_h (cm ² /V s)	10	10	25	5.85×10^2	12
Shallow uniform donor density, N_D (1 cm ⁻³)	2×10^{19}	1×10^{21}	0	0	0
Shallow uniform acceptor density, N_A (1 cm ⁻³)	0	0	1×10^{15}	1×10^{16}	1×10^{19}
Reference	[26]	[27]	[28]	[29]	[30]

**Fig. 1.** Workflow diagram illustrating the step-by-step procedure used in SCAPS-1D for solar cell simulation.

Despite the advantages of inorganic PVK, several technical challenges remain, including high defect densities, non-radiative recombination, inefficient charge extraction, and interfacial energy level mismatches [20]. These issues can significantly affect device performance and stability. Optimizing materials and device architectures through experimental methods is time-consuming and resource-intensive [21]. Therefore, numerical simulation has become a crucial tool for guiding device design and accelerating development [22]. Among the available simulation tools, SCAPS-1D (Solar Cell Capacitance Simulator – 1D) software, originating from the University of Ghent, is commonly employed to simulate thin-film solar cells [23]. It enables detailed analysis of charge carrier dynamics, energy band alignment, recombination mechanisms, and the influence of defects under varying operating conditions [24].

**Fig. 2.** The key physical laws and equations implemented in SCAPS-1D simulations.

Using SCAPS-1D, we modeled a tandem-inspired all-inorganic PSCs featuring a dual-layer absorber structure, combining CsPbI₃ as the upper absorber and CsSnI₃ as the lower absorber. This configuration aims to broaden the spectral response and improve overall device efficiency by leveraging the complementary photonic and electrical properties of the two compounds. This simulation explored both hole transport layer (HTL)-free and HTL-containing architectures, with various back-contact materials including gold (Au), silver (Ag), carbon, and the low-cost, sustainable semiconductor Cu₂ZnSnS₄ (CZTS). The results demonstrated that high PCEs can be achieved even in the absence of organic HTLs, offering a simplified and environmentally benign design. This study PVSK insights into optimising all-inorganic tan-PSCs and supports their potential as scalable, efficient, and eco-friendly photovoltaic solutions.

2. Methodology and modelling

2.1. SCAPS-1D modelling

The numerical simulation of PSCs was performed using SCAPS-1D. The modelling process begins by launching the SCAPS-1D software and defining the problem setup, which includes selecting the appropriate device structure [25]. Subsequently, input parameters such as layer thicknesses, doping concentrations, bandgap energies, mobility values, and defect densities are entered for each layer in the solar cell structure. These input parameters, detailed in Table 1, were chosen based on literature values and experimental estimates to ensure realistic modelling conditions. Following this, illumination conditions are configured to simulate the illuminated state under the standard AM1.5G solar spectrum. The simulation is then executed using the “Calculate: single shot” function to generate J-V characteristics, quantum efficiency (QE), and additional electrical parameters. Fig. 1 shows the step-by-step approach that enables how changes in material attributes and layer configurations influence device operation, promoting effective solar cell optimization design without the need for extensive experimental trials.

2.2. Equations and laws Governing SCAPS-1D

Fig. 2 illustrates the key physical laws and equations implemented in SCAPS-1D simulations, which model the electrical behavior of thin-film and PSCs. These laws are fundamental to understanding and designing efficient photovoltaic devices. Poisson’s Equation (1) is essential in SCAPS-1D simulations, as it governs the electrostatic potential

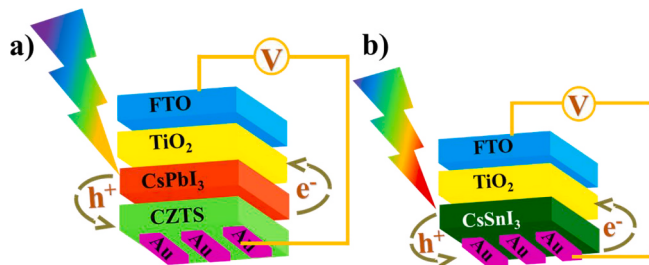


Fig. 3. The schematic device architecture for a) CsPbI₃ is FTO/TiO₂/CsPbI₃/CZTS/Au, b) CsSnI₃ is FTO/TiO₂/CsSnI₃/Au.

distribution across the solar cell [26–28]. This equation links the spatial distribution of the electric field to the local charge density, accounting for free carriers (electrons and holes), ionized dopants, and other charge contributors. By solving Poisson's equation, SCAPS-1D can determine how the internal electric field is shaped within the stacking of functional layers, fundamental to achieving efficient charge generation and flow [29–31].

$$\frac{d}{dx} \left(-\epsilon(x) \frac{d\phi}{dx} \right) = q[p(x) - n(x) + N_d^+(x) - N_a^-(x)] \quad (1)$$

Here, $\phi(x)$ expresses the electrostatic potential relative to position x ; q represents the fundamental charge (1.602×10^{-19} C); ϵ is the dielectric constant; $p(x)$ and $n(x)$ are the concentrations of holes and electrons; N_a^- and N_d^+ refer to the ionized acceptor and donor densities.

The electron continuity equation (2) is vital in understanding and

optimising charge transport in PSCs. It ensures electron charge conservation by relating the electron current density divergence to the effective generation-recombination processes inside the device [32].

$$\frac{\partial j_n}{\partial x} = q \left(R_n - G + \frac{\partial n}{\partial t} \right) \quad (2)$$

where j_n refers to how much current is carried by electrons, G is the number of carriers created by absorbing light. R_n is the rate at which those electrons are lost through recombination. This equation enables the analysis of how efficiently photo-generated electrons are transported and collected across different layers, including the photoactive layer and the ETL. The hole continuity equation (3) is a fundamental component in the modelling of PSCs, ensuring the conservation of hole carriers within the device [33].

$$\frac{\partial j_p}{\partial x} = -q \left(R_p - G + \frac{\partial p}{\partial t} \right) \quad (3)$$

Here, j_p means the density of hole current, G is the rate at which light produces electron-hole pairs, R_p is the recombination rate of holes, and q is the elementary charge [34]. The electron current density equation (4) and (5) describes how electrons and holes move through the device under the combined effects of diffusion and drift mechanisms [35].

$$j_n = D_n \frac{dn}{dx} + \mu_n n \frac{d\phi}{dx} \quad (4)$$

$$j_p = D_p \frac{dp}{dx} + \mu_p p \frac{d\phi}{dx} \quad (5)$$

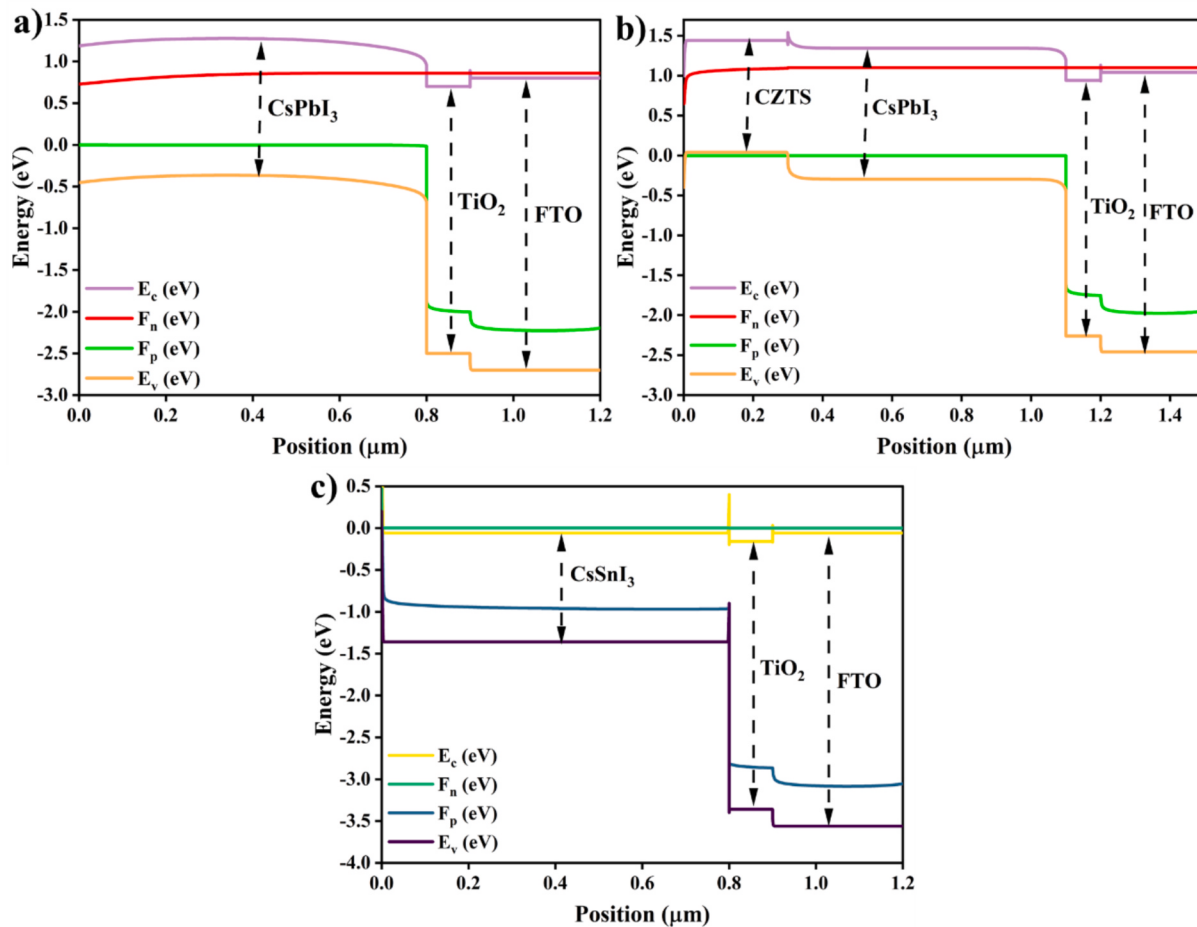


Fig. 4. Energy band diagrams of simulated devices: (a) CsPbI₃ without HTL, (b) CsPbI₃ with CZTS HTL, and (c) CsSnI₃ without HTL.

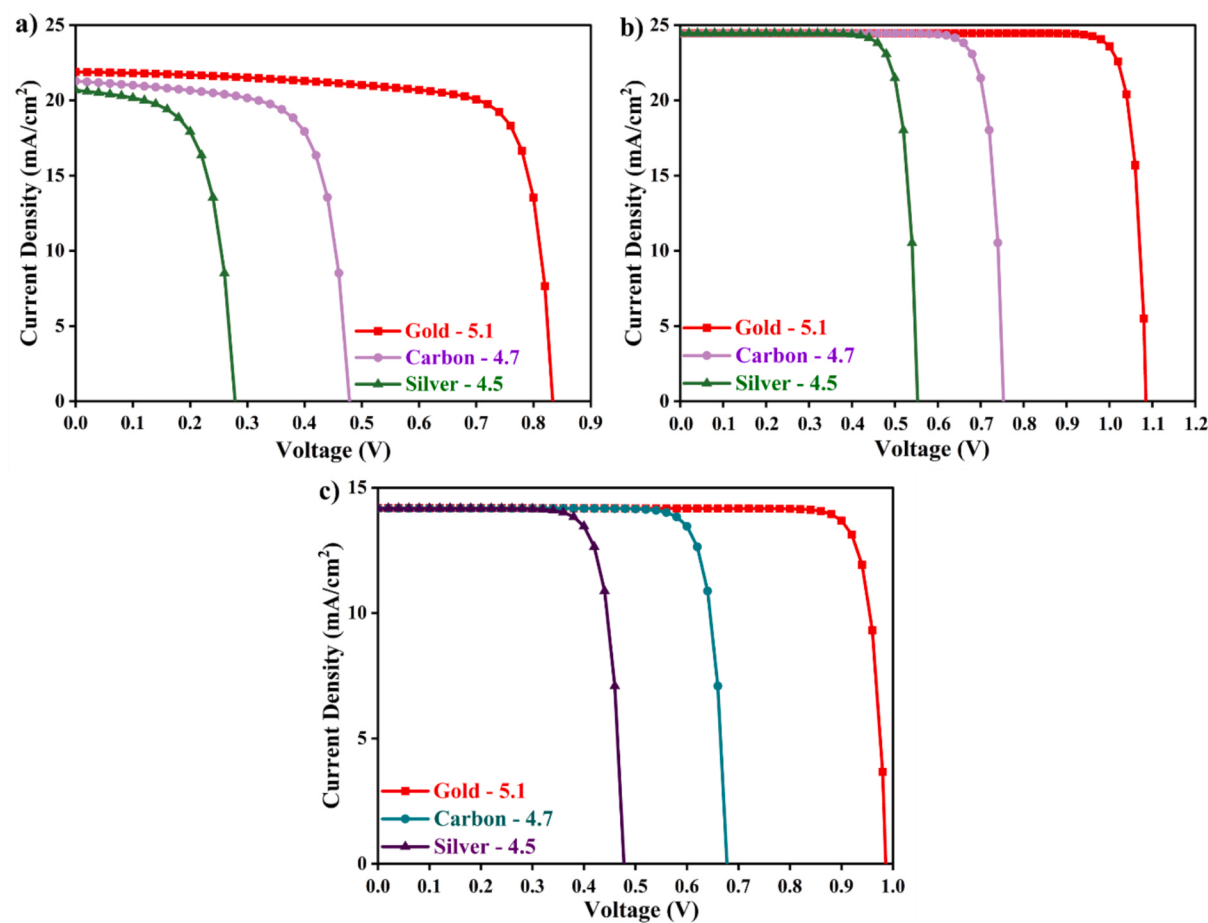


Fig. 5. Simulated J-V curves of PSCs: (a) CsPbI₃ without HTL, (b) CsPbI₃ with CZTS as HTL, and (c) CsSnI₃ without HTL.

Table 2

Electrical output parameters of PSCs subjected to different back contacts, CsPbI₃ devices without and with CZTS as HTL, and CsSnI₃ devices without HTL.

Perovskite	Back contact	HTL	V _{oc} (V)	J _{sc} (mA/cm ²)	FF (%)	PCE (%)
CsPbI ₃	Gold (Au)	W/O	0.834	21.89	78.02	14.26
		W	1.08	24.46	88.98	23.64
	Carbon (C)	W/O	0.47	21.28	70.59	7.20
		W	0.75	24.45	85.44	15.76
	Silver (Ag)	W/O	0.27	20.6	62.85	3.62
		W	0.55	24.45	81.76	11.08
CsSnI ₃	Gold (Au)	—	0.98	14.81	88.01	12.33
	Carbon (C)	—	0.67	14.17	84.06	8.08
	Silver (Ag)	—	0.47	14.17	79.54	5.39

Here, j_n and j_p represent charge carrier current densities, D_n and D_p are the diffusion coefficients, μ_n and μ_p denote the charge carrier mobilities, n and p represent the concentrations of electrons and holes, and $d\phi/dx$ refers electric potential gradient. The diffusion terms arise from concentration gradients established by photogenerated carriers that naturally diffuse from regions of higher concentration to lower concentration. The drift terms represent the motion of carriers acted upon by the device's internal electric field.

Beer-Lambert law and the radiative recombination law play essential roles in modelling light absorption and carrier dynamics, respectively [36]. The Beer-Lambert law governs how light is absorbed across the PVK layer. This law underpins SCAPS-1D's simulation of carrier

generation, where photons penetrating the absorber layer are absorbed, giving rise to charge carriers responsible for photocurrent. The radiative recombination law quantifies the loss of photo-generated carriers due to radiative recombination [37]. This process is intrinsic to the material and depends on carrier densities and energy band properties. Shockley-Read-Hall (SRH) recombination equation (6) happens via localized trap levels or defect states that exist within the bandgap of a semiconductor [38]. These trap states are typically introduced during fabrication due to crystal imperfections, impurities, or interface defects [39].

$$R_{SRH} = \frac{n_p - n_i^2}{\tau_p(n + n_1) + \tau_n(p + p_1)} \quad (6)$$

Here, n and p represent the concentrations of electrons and holes, n_i refers to the intrinsic carrier density; τ_n and τ_p represent the charge carrier lifetimes; and n_1 and p_1 denote the carrier concentrations corresponding to the trap energy level in equilibrium with the bands corresponding to conduction and valence. All these relationships are incorporated into SCAPS-1D to simulate the behavior and efficiency of solar cells [40].

3. Results and Discussion

3.1. CsPbI₃ and CsSnI₃ perovskite solar cell

A PSC was modelled using both CsPbI₃ and CsSnI₃ as absorber layers to investigate the impact of device architecture and back contact selection on photovoltaic performance. SCAPS-1D was utilized to execute the simulations, considering configurations both with and without an

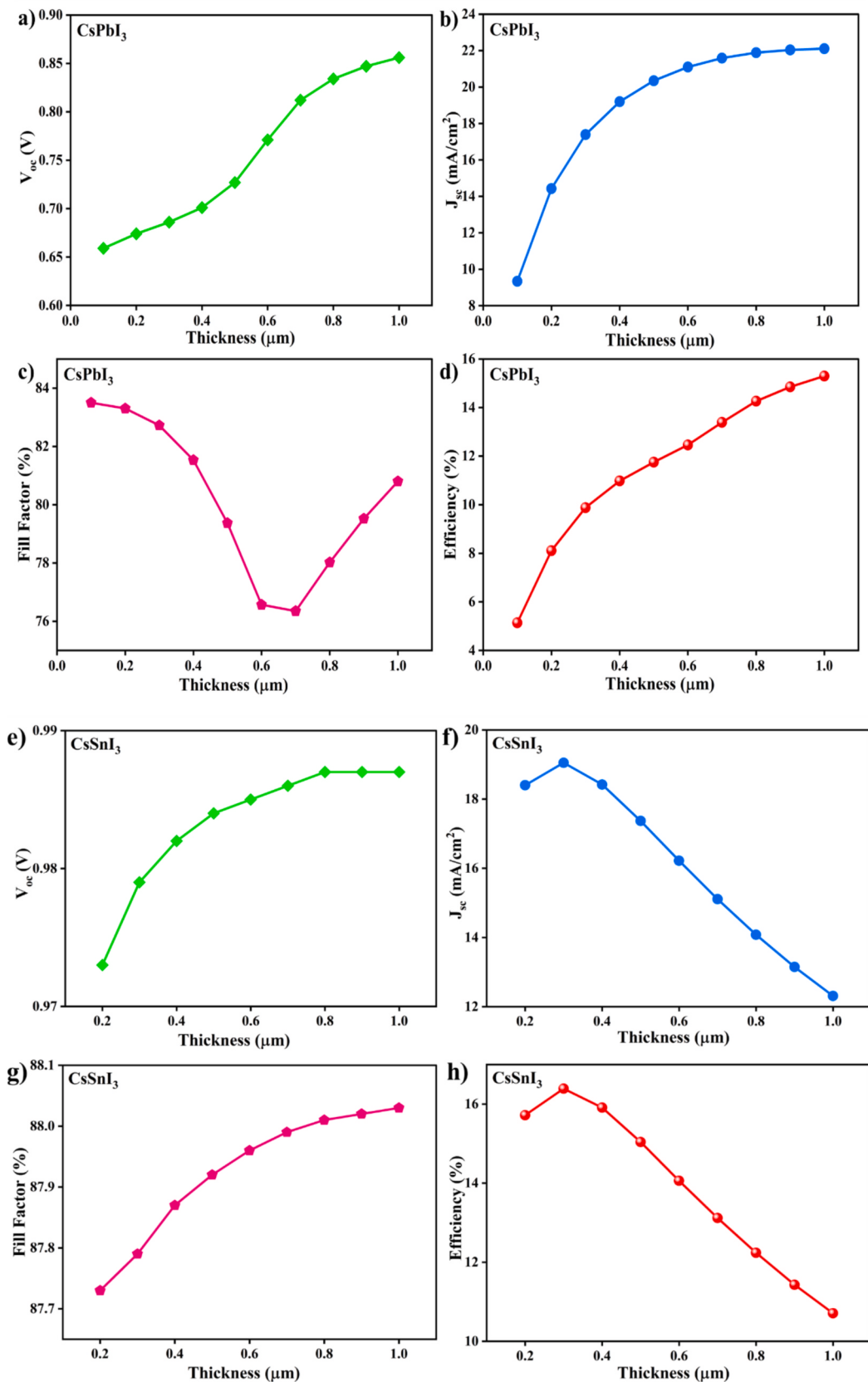


Fig. 6. Simulated photovoltaic performance of PSCs: (a-d) CsPbI_3 with varying absorber thickness (0.1–1.0 μm); (e-h) CsSnI_3 with varying thickness (0.2–1.0 μm), showing optimal efficiency at thinner layers.

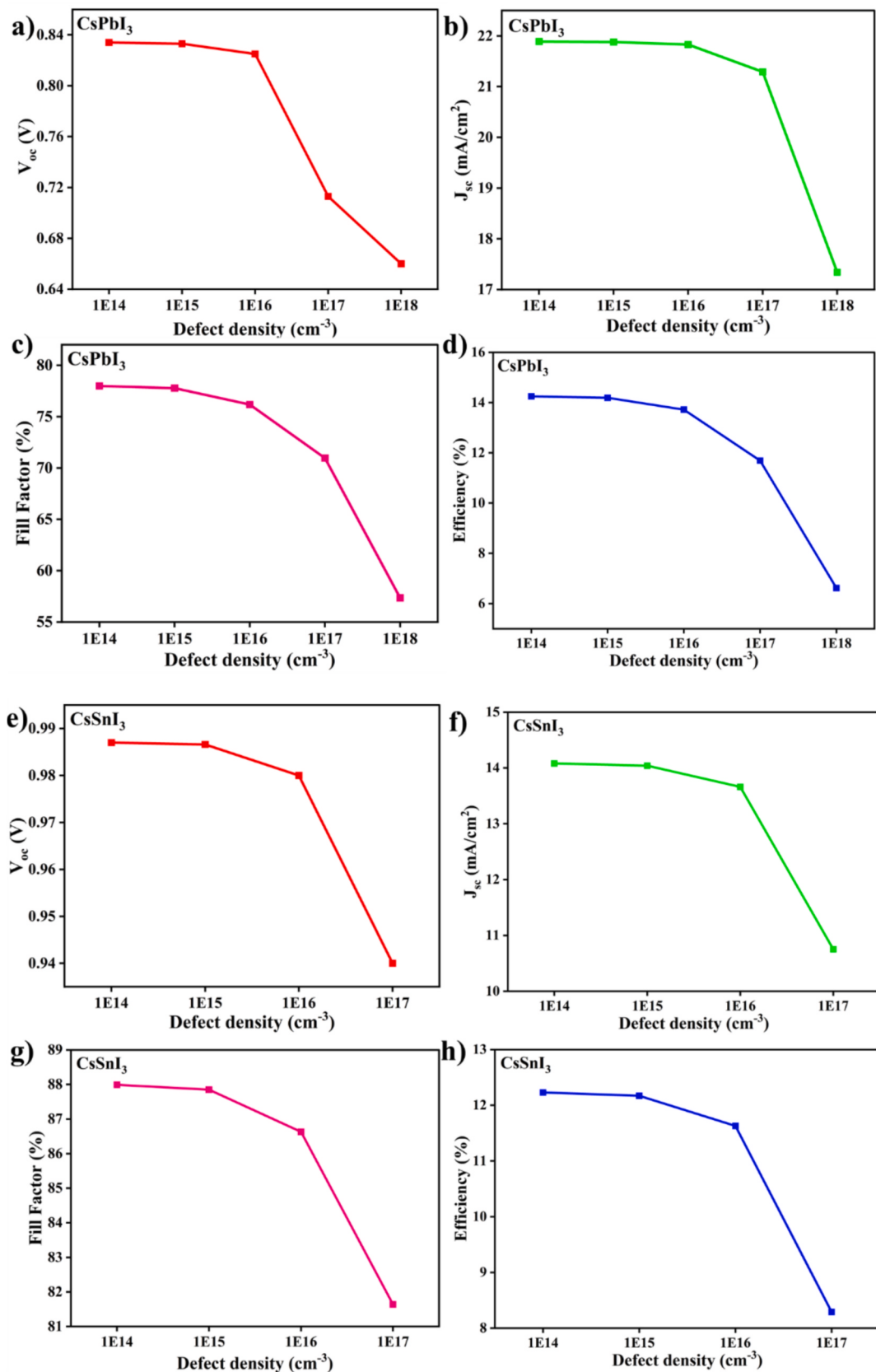


Fig. 7. Simulated photovoltaic performance with varying absorber defect density: (a-d) CsPbI_3 (1×10^{14} to $1 \times 10^{18} \text{ cm}^{-3}$), (e-h) CsSnI_3 (1×10^{14} to $1 \times 10^{17} \text{ cm}^{-3}$).

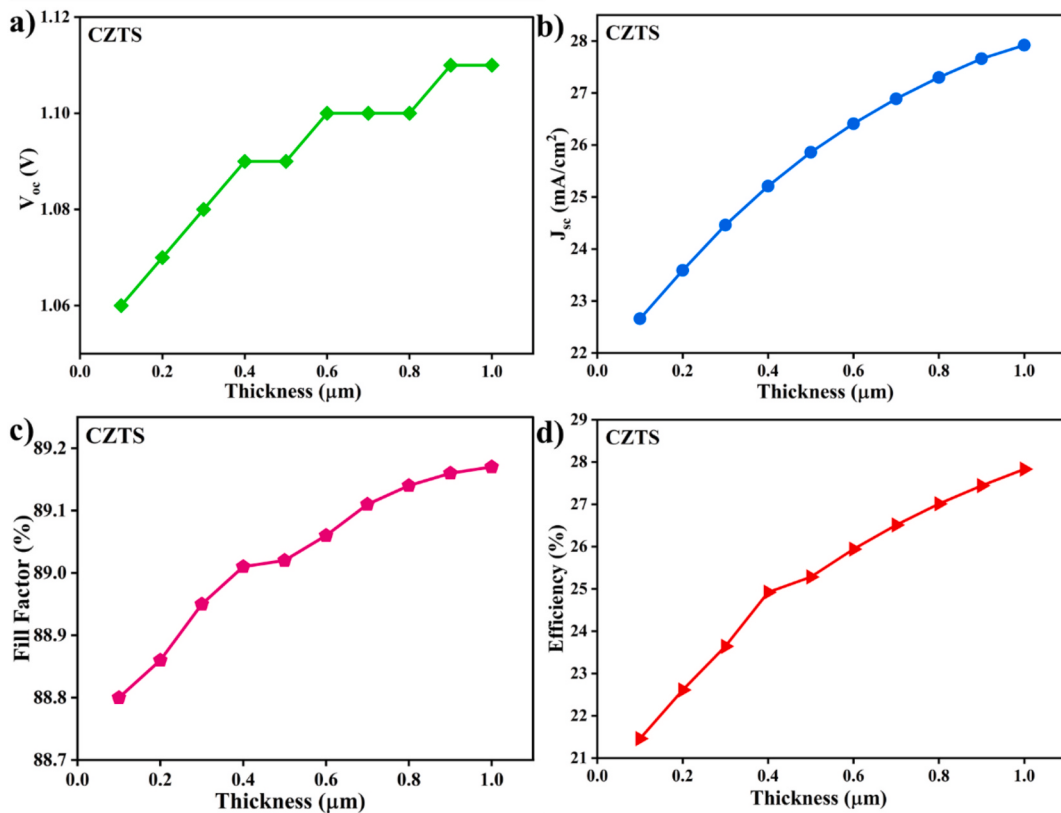


Fig. 8. Impact of Thickness of the hole transport layer CZTS on photovoltaic performance: a) V_{oc} (V), b) J_{sc} (mA/cm²), c) Fill factor (%), d) PCE (%).

HTL and incorporating various back contact materials such as Au, Ag, and carbon. Fig. 3a and 3b illustrate the schematic structures of the CsPbI₃ and CsSnI₃-based devices. The study systematically analysed key parameters, including energy band alignment, J-V performance, IPCE measurements, and defect density. While CsPbI₃ offers a relatively wide bandgap and high thermal stability, CsSnI₃, with its narrower bandgap (~1.3 eV) and strong near-infrared absorption, is particularly suited for bottom cell applications in tandem PSCs (tan-PSCs). Moreover, its lead-free composition and favorable opto-electronic properties make CsSnI₃ a promising and Sustainable replacement for standard lead-based PVSK materials.

3.1.1. Energy band diagram (EBD) of CsPbI₃ and CsSnI₃

Efficient charge extraction in both CsPbI₃ and CsSnI₃-based PSC is dictated by the atomic-scale alignment of electronic states at their interfaces. In CsPbI₃ Antibonding Pb 6p states give rise to the conduction band minimum, and the valence band maximum is created by hybridised Pb 6 s-I 5p orbitals; when this perovskite contacts a metallic Au back electrode without an intervening HTL, the resulting valence-band mismatch creates a sharp energy cliff that traps holes and enhances Energy-loss recombination pathways as depicted in Fig. 4a, the misalignment leads to a localised electrostatic field and inefficient charge extraction. Introducing CZTS as an HTL reconfigures the interface; its Cu 3d-S 3p-derived VBM aligns well with that of CsPbI₃, providing orbital continuity, suppressing interfacial defect formation, and flattening the hole quasi-Fermi level so that holes can delocalize and extract with minimal loss (Fig. 4b). In contrast, CsSnI₃, whose VBM is dominated by I 5p-Sn 5 s bonding and CBM by Sn 5p states, possesses a narrower ~ 1.3 eV bandgap that efficiently captures near-infrared light. As shown in Fig. 4c, at the TiO₂/CsSnI₃ junction, the TiO₂ conduction band lies below that of CsSnI₃, enabling downhill electron transfer, while the valence-band offset blocks holes, establishing a field that drives electrons toward TiO₂ and holes toward the Au back contact. The

resulting band bending and quasi-Fermi-level splitting within CsSnI₃ underpin its open-circuit voltage, whereas the graded CZTS/CsPbI₃ interface facilitates ballistic or thermionic hole transport, illustrating how tailored band alignment and orbital compatibility at each junction fundamentally enhance photovoltaic performance.

3.1.2. Simulated J-V characteristics

The J-V characteristics presented in Fig. 5a (for CsPbI₃ devices) and Fig. 5b (for CsSnI₃ devices) underscore the pivotal role of interfacial engineering and back contact selection in dictating the photovoltaic performance of PSCs. In the FTO/TiO₂/CsPbI₃/Au structure, although strong Pb 6p and I 5p orbital hybridisation facilitates efficient light absorption and charge generation, the poor valence band alignment with Au (work function ~ 5.1 eV) leads to a hole extraction barrier and increased trap-assisted recombination at the PVSK interface. This is exacerbated by the absence of a hole transport layer, which permits hole accumulation and loss of charge carriers at undercoordinated Pb²⁺ and iodide vacancy sites. However, when CZTS is introduced as an HTL between CsPbI₃ and Au (Fig. 5), its valence band (~5.2 eV) forms a cascade alignment with CsPbI₃, enabling more efficient hole extraction via Cu 3d and S 3p orbitals, while simultaneously blocking electrons and passivating interfacial defects. This results in enhanced V_{oc} , FF, and PCE, as confirmed in Table 2. On the other hand, back contacts like Ag and carbon lead to inferior performance due to their lower work functions (~4.5 eV and ~ 4.7 eV, respectively), which increase hole extraction barriers and promote recombination, with Ag also risking diffusion into the PVSK layer and defect formation. Similarly, in CsSnI₃ devices without HTLs (Fig. 5b), Au emerges as the most effective back contact, yielding a PCE of 12.33 %, owing to its favorable energy alignment and inert surface, which minimises interfacial defects and supports high quasi-Fermi level splitting. In contrast, carbon-based devices show moderate performance due to higher contact resistance and less efficient hole extraction, while Ag-based devices exhibit the lowest PCE (5.39 %)

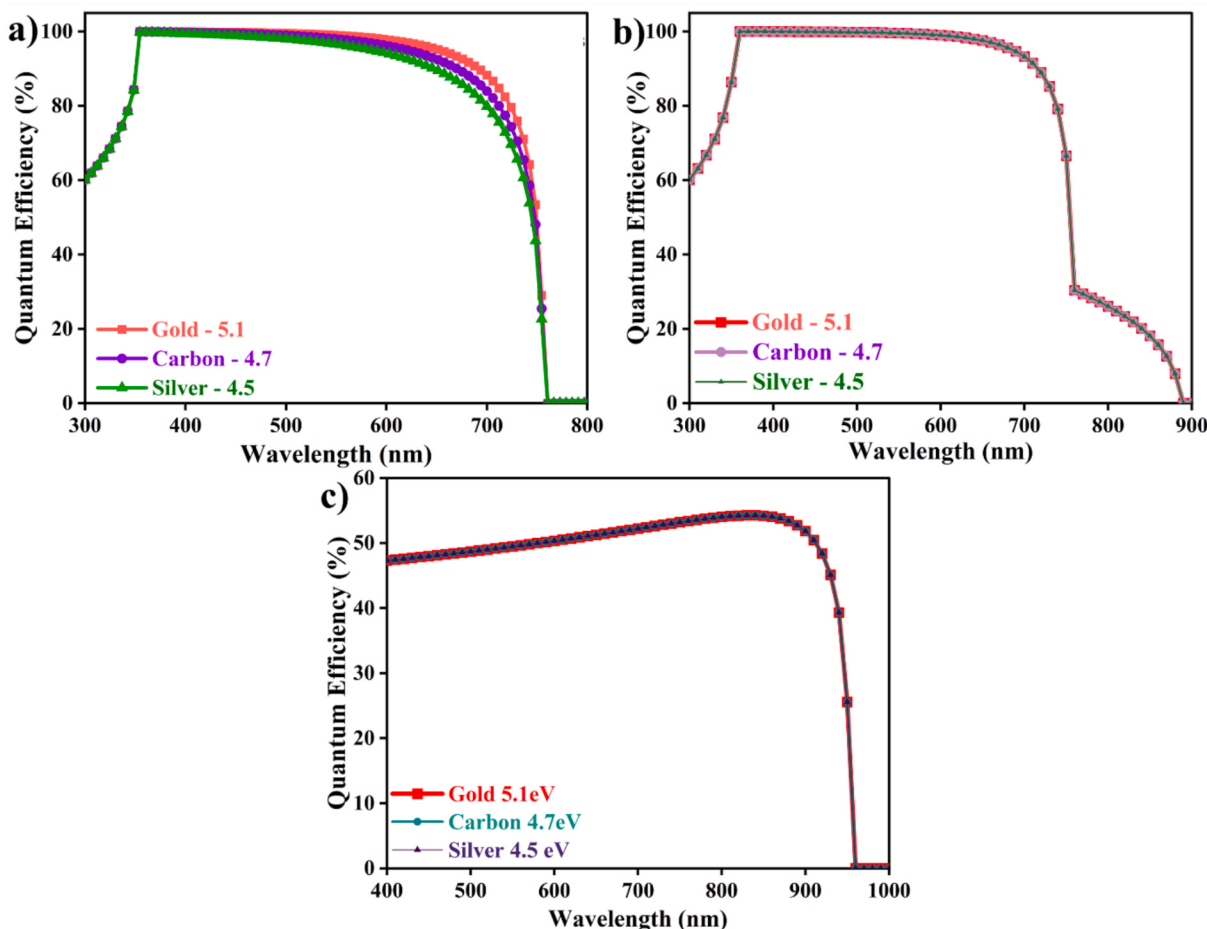


Fig. 9. Simulated quantum efficiency (QE) spectra of PSCs: (a) CsPbI₃ without HTL, (b) CsPbI₃ with CZTS as HTL, (c) CsSnI₃ without HTL.

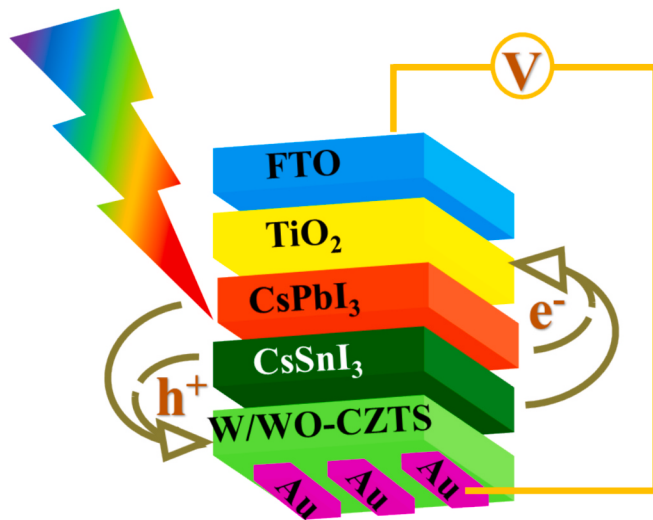


Fig. 10. Schematic structure of Tandem CsPbI₃/CsSnI₃ device architecture consists of FTO/TiO₂/CsPbI₃/CsSnI₃/CZTS/Au.

and V_{oc} (0.47 V) due to Schottky barrier formation and Ag-induced trap states, as detailed in Table 2.

3.1.3. Effect of the perovskite layer thickness

Fig. 6 demonstrates how variations in the PVK layer thickness affect the photovoltaic performance of CsPbI₃ and CsSnI₃ PSCs, respectively,

both employing the FTO/TiO₂/absorber/Au architecture. In the case of CsPbI₃ (Fig. 6a-d), increasing the PVK absorber thickness from 0.1 μm to 1.0 μm leads to a steady enhancement in all key parameters V_{oc} rises from 0.659 to 0.856 V, J_{sc} increases from 9.34 to 22.11 mA/cm², and PCE peaks at 15.30 % for 1.0 μm indicating improved light harvesting and carrier collection efficiency. While FF remains relatively stable with a slight dip around 0.6 μm due to recombination, it improves again beyond 0.8 μm, confirming that optimised thickness supports better device performance by balancing absorption and recombination. In contrast, the CsSnI₃-based device (Fig. 6e-h) exhibits optimal performance at a lower thickness of 0.3 μm, where a PCE of 16.39 %, V_{oc} of 0.979 V, and J_{sc} of 19.05 mA/cm² are achieved. This thin-film regime benefits from efficient carrier diffusion, low recombination, and strong electric fields at the TiO₂/CsSnI₃ interface. Beyond a certain thickness of 0.4 μm, performance declines due to enhanced bulk recombination, driven as a result of Sn²⁺ being oxidized to Sn⁴⁺ and the formation of deep-level trap states like tin vacancies and iodine interstitials. By 1.0 μm, the PCE drops to 10.71 % due to suppressed quasi-Fermi level splitting and reduced carrier lifetimes.

3.1.4. Effect of perovskite layer defect density

Fig. 7 demonstrates the influence of varying defect density (DD-N_t) on the photovoltaic performance of CsPbI₃ and CsSnI₃ PSCs, both using the FTO/TiO₂/absorber/Au device configuration. In the case of CsPbI₃ (Fig. 7a-d), increasing the DD from $1 \times 10^{14} \text{ cm}^{-3}$ to $1 \times 10^{18} \text{ cm}^{-3}$ leads to a noticeable drop across all critical metrics. At the least N_t ($1 \times 10^{14} \text{ cm}^{-3}$), the device exhibits high V_{oc} = 0.834 V, J_{sc} = 21.89 mA/cm², FF = 77.99 %, and PCE = 14.25 %. However, at $1 \times 10^{18} \text{ cm}^{-3}$, V_{oc} drops to 0.66 V and PCE falls to 6.62 %, primarily

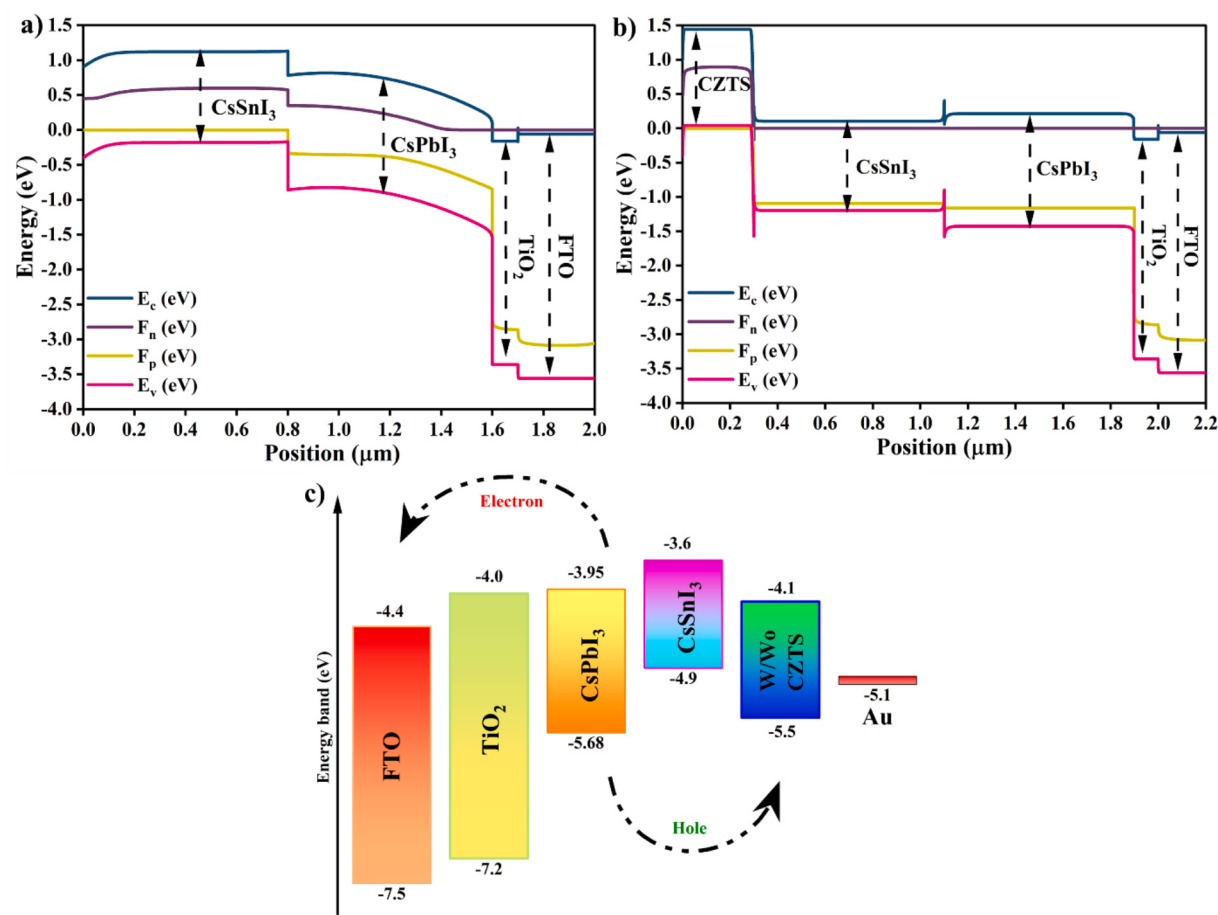


Fig. 11. Energy band diagrams of a tan-PSC (a) without HTL, (b) with CZTS as an HTL, (c) band alignment.

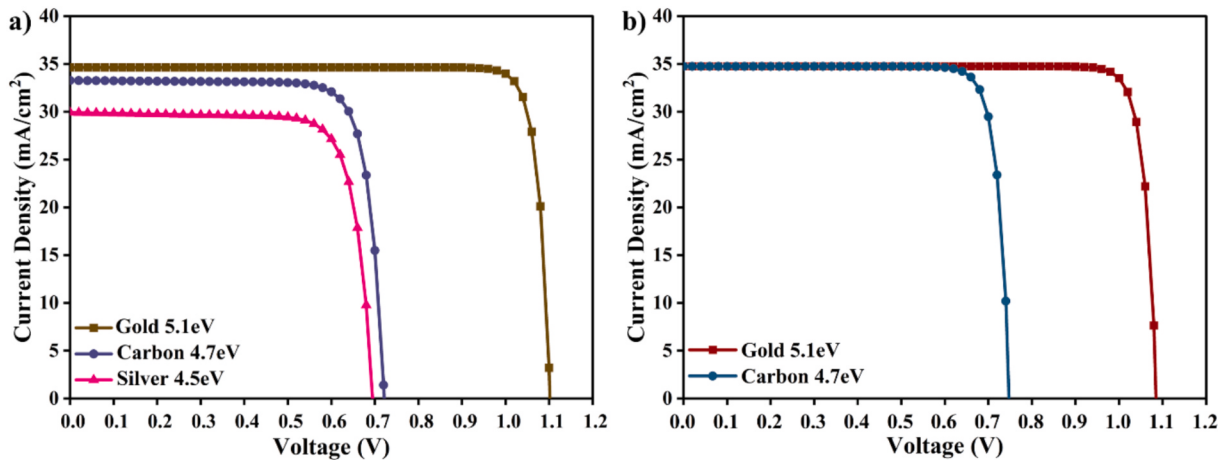


Fig. 12. Simulated J-V curve for CsPbI₃/CsSnI₃ tan-PSC a) without CZTS b) with CZTS as an HTL.

due to increased non-radiative recombination caused by deep-level trap states arising from halide vacancies, interstitials, or antisite defects. These trap states, especially those located mid-gap, facilitate Shockley-Read-Hall-Hall (SRH) recombination, notably shortening carrier lifetimes and impairing charge extraction. Similarly, in CsSnI₃ devices (Fig. 7e-h), a low DD (1×10^{14} - 10^{15} cm^{-3}) maintains strong photovoltaic performance ($V_{oc} \approx 0.987 \text{ V}$, FF $\approx 88\%$, PCE $> 12\%$), with minimal recombination. However, as N_t increases to $1 \times 10^{15} \text{ cm}^{-3}$, the formation of deep-level imperfections like Sn vacancies (V_{Sn}) and interstitial iodine atoms (I_i) accelerates recombination, leading to a drop

in carrier lifetimes and quasi-Fermi level splitting. At $1 \times 10^{17} \text{ cm}^{-3}$, this degradation intensifies, reducing PCE to 8.29 %, and beyond this point, simulation convergence fails due to electronic instability. These findings confirm that maintaining low defect densities is crucial in both lead- and tin-based PVSKs to promote effective charge transport, extended carrier lifetimes, and optimal device efficiency.

3.1.5. Impact of the hole transport layer (CZTS) thickness

The influence of CZTS layer thickness on the performance of CsPbI₃ PSCs with the device structure FTO/TiO₂/CsPbI₃/CZTS/Au is illustrated

Table 3

Photovoltaic parameters for different back contacts in $\text{CsPbI}_3/\text{CsSnI}_3$ tan-PSC without and with HTL.

Back contact	HTL	V_{oc} (V)	J_{sc} (mA/cm^2)	FF (%)	PCE (%)
Gold (Au)	W/O	1.10	34.38	89.06	33.79
	W	1.08	34.50	88.94	33.32
Carbon (C)	W/O	0.72	33.03	80.99	19.29
	W	0.74	34.50	85.36	22.04
Silver (Ag)	W/O	0.69	29.68	78.62	16.22
	W	—	—	—	—

in Fig. 8 (a-d). The CZTS thickness was varied from 0.1 μm to 1.0 μm , and a steady improvement in photovoltaic parameters was observed with increasing thickness. The V_{oc} increased from 1.06 to 1.11 V, while the J_{sc} rose from 22.66 to 27.92 mA/cm^2 . Correspondingly, the PCE improved significantly from 21.46 % to 27.83 %. Enhanced performance is linked to favorable energy level alignment between CZTS and CsPbI_3 , which supports efficient hole transport and reduces recombination at the interface. Thicker CZTS layers also act as effective recombination barriers, minimising trap-assisted carrier losses and ensuring that the photogenerated holes are efficiently transported to the back contact. As demonstrated in Fig. 8, the optimised CZTS thickness enhances overall charge collection and device stability, highlighting its crucial role in high-performance PSCs.

3.1.6. Quantum efficiency (QE) analysis

The QE spectra of CsPbI_3 and CsSnI_3 PSCs reveal distinct insights into charge collection behavior and interfacial performance across different device architectures. In the case of CsPbI_3 devices, those lacking an HTL

show high QE values (>95 %) in the 400–650 nm range, but experience a steep decline beyond 700 nm, especially for silver and carbon electrodes, due to poor valence band alignment and increased interfacial recombination at the $\text{CsPbI}_3/\text{metal}$ interface. In contrast, devices incorporating a CZTS HTL exhibit enhanced QE across the full spectral range, maintaining values > 90 % up to ~ 780 nm and showing reduced sensitivity to back contact materials. The observed performance gain results from the creation of an efficient heterojunction between CZTS and CsPbI_3 , which facilitates hole extraction and minimises non-radiative losses, ultimately translating to higher PCE. Meanwhile, CsSnI_3 devices display consistent QE spectra across 400–950 nm with peak values near 55 %, indicating effective photogeneration and carrier collection spanning the visible and near-infrared wavelengths. The sharp drop in QE beyond 950 nm corresponds to the material's bandgap (~1.3 eV), where photon energy becomes insufficient to generate charge carriers. These trends, as shown in Fig. 9a-b (CsPbI_3) and Fig. 9c (CsSnI_3), emphasize the significance of optimizing both interfacial properties and spectral response for achieving high-performance PSCs.

3.2. $\text{CsPbI}_3/\text{CsSnI}_3$ Tandem-Perovskite solar cell (tan-PSC)

A tan-PSC was modelled with architecture FTO/TiO₂/ $\text{CsPbI}_3/\text{CsSnI}_3/\text{CZTS}/\text{Au}$, as shown in Fig. 10, aiming to combine the complementary optical properties of two lead and tin-based PVSks. In this structure, CsPbI_3 serves as the wide bandgap top absorber, efficiently harvesting high-energy photons, while CsSnI_3 , with its narrower bandgap (~1.3 eV), operates as the bottom light-harvesting layer to utilise near-infrared light. A simulated reference device was also analysed without the CZTS interlayer, enabling direct evaluation of the

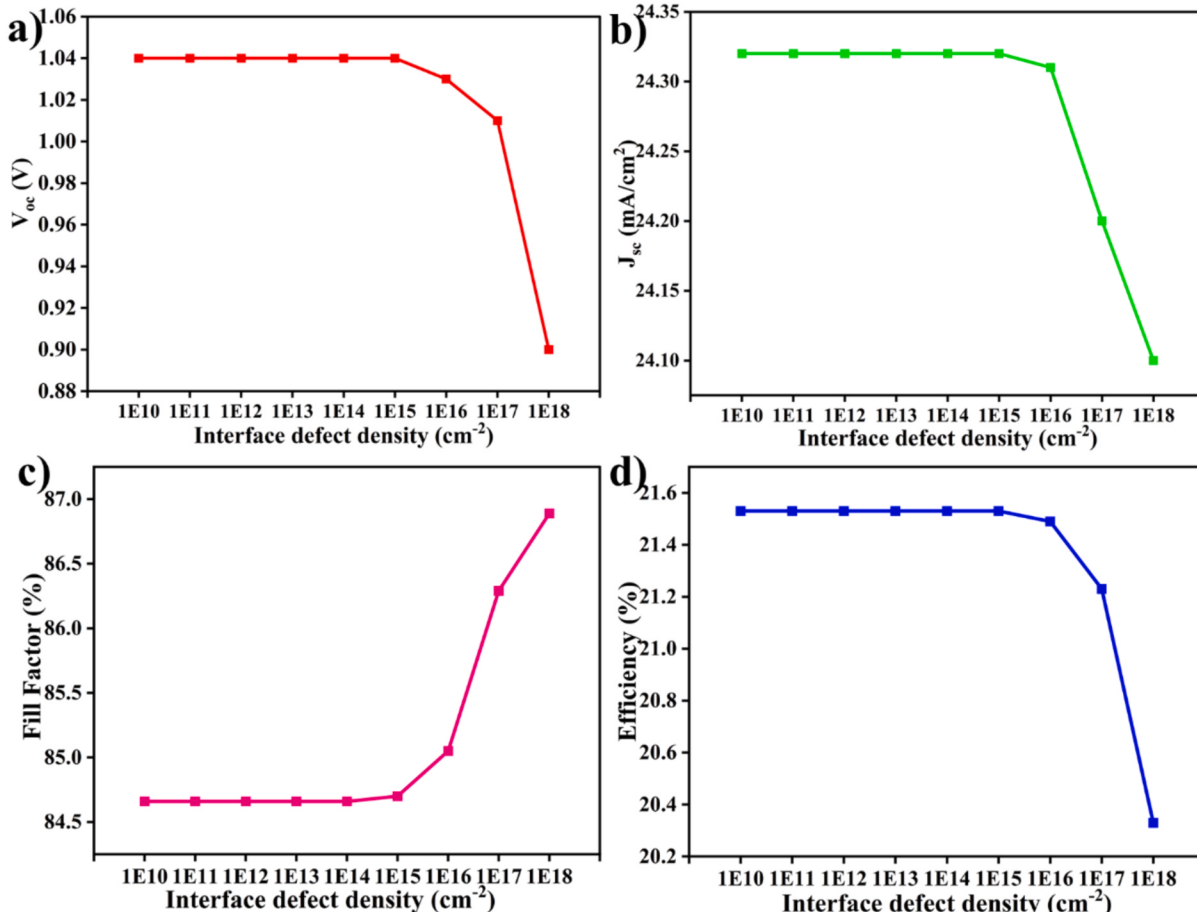


Fig. 13. Effect of Interface DD of $\text{TiO}_2/\text{CsPbI}_3$ on photovoltaic performance: a) V_{oc} (V), b) J_{sc} (mA/cm^2), c) Fill factor (%), d) PCE (%).

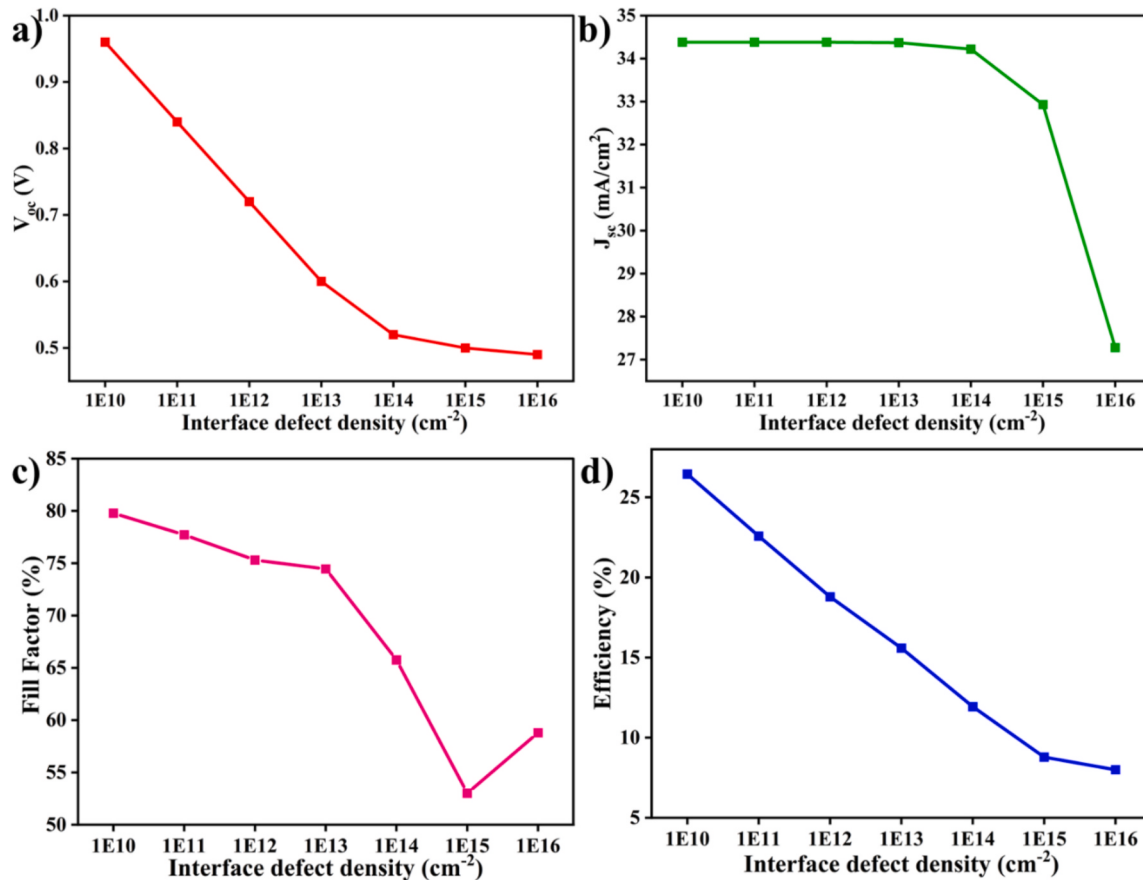


Fig. 14. Impact of Interface DD of $\text{CsPbI}_3/\text{CsSnI}_3$ on photovoltaic parameters: a) V_{oc} (V), b) J_{sc} (mA/cm^2), c) Fill factor (%), d) PCE (%).

absorber layers' performance. The combination of CsPbI_3 and CsSnI_3 offers a favorable band alignment and efficient photogeneration across a broad spectral range, with CsSnI_3 contributing significantly to the infrared response, owing to its strong light absorption and superior carrier mobility.

3.2.1. Energy band diagram (EBD) of tandem PSC

The EBD of tan-PSCs with the architecture FTO/TiO₂/CsPbI₃/CsSnI₃/CZTS/Au, as shown in Fig. 11(a-b), was simulated both with and without the CZTS HTL. The band structures are shaped by the orbital interactions within the perovskite layers Pb 6p and I 5p in CsPbI_3 , and Sn 5p and I 5p in CsSnI_3 , which define the conduction and valence band edges. In both cases, efficient energy level alignment between the CsPbI_3 and CsSnI_3 layers enables effective absorption across a broad spectrum and promotes charge separation. The inclusion of CZTS introduces a slight improvement in valence band alignment at the CsSnI_3/Au interface, potentially reducing recombination by facilitating hole extraction. However, the PCE remains nearly the same, 33.79 % without CZTS and 33.32 % with CZTS, indicating that the intrinsic quality and energy level compatibility of the $\text{CsPbI}_3/\text{CsSnI}_3$ stack already ensure highly efficient charge transport and collection. The marginal difference in efficiency suggests that, although CZTS provides slight interfacial smoothing and improved band alignment at the CsSnI_3/Au interface, the perovskite-perovskite tandem architecture is inherently well-optimised, achieving high performance even in the absence of an additional hole-selective interlayer. The EBD in Fig. 11(c) illustrates the alignment of the FTO/TiO₂/CsPbI₃/CsSnI₃/CZTS/Au heterostructure, highlighting the carrier transport mechanism in the device. Each layer's CBM and VBM are referenced to the vacuum level.

3.2.2. Simulated J-V characteristics

The J-V characteristics of the tan-PSCs, as shown in Fig. 12, and the corresponding photovoltaic parameters summarized in Table 3, highlight the impact of back contact materials and the inclusion of a CZTS HTL on device performance. The tandem architecture FTO/TiO₂/CsPbI₃/CsSnI₃/(CZTS)/back contact demonstrates efficient charge separation and light harvesting by combining the wide-bandgap CsPbI_3 and the narrow-bandgap CsSnI_3 , enabling broader spectral absorption and enhanced current generation. The best performance was observed incorporating Au as the bottom electrode, achieving a PCE of 33.79 % without CZTS and 33.32 % with CZTS, as shown by the high J_{sc} (~34.5 mA/cm^2) and FF (~89 %), indicating excellent charge transport with suppressed interfacial recombination. The device with carbon as the back contact exhibited a notable increase in PCE from 19.29 % (without CZTS) to 22.04 % (with CZTS), driven by improvements in V_{oc} and FF, confirming the beneficial role of CZTS in enhancing hole extraction. The cell with Ag showed the lowest performance (PCE – 16.22 %) without CZTS, and the simulation with CZTS failed to converge, suggesting severe interfacial mismatches or instability. Overall, Fig. 12 and Table 3 confirm that the tandem structure offers significant advantages, including voltage addition, extended light absorption, and improved charge collection, while the choice of back contact and interfacial layers like CZTS critically influences recombination dynamics and overall efficiency.

3.2.3. Effect of TiO₂/CsPbI₃ interfacial defect density

Fig. 13(a-d) illustrates how varying the interface DD at the TiO₂/CsPbI₃ junction from 1×10^{10} to $1 \times 10^{18} \text{ cm}^{-2}$, affects device performance. The key photovoltaic parameters show minimal variation up to a defect density of $1 \times 10^{15} \text{ cm}^{-2}$. This suggests minimal interfacial recombination and efficient charge extraction at lower defect levels.

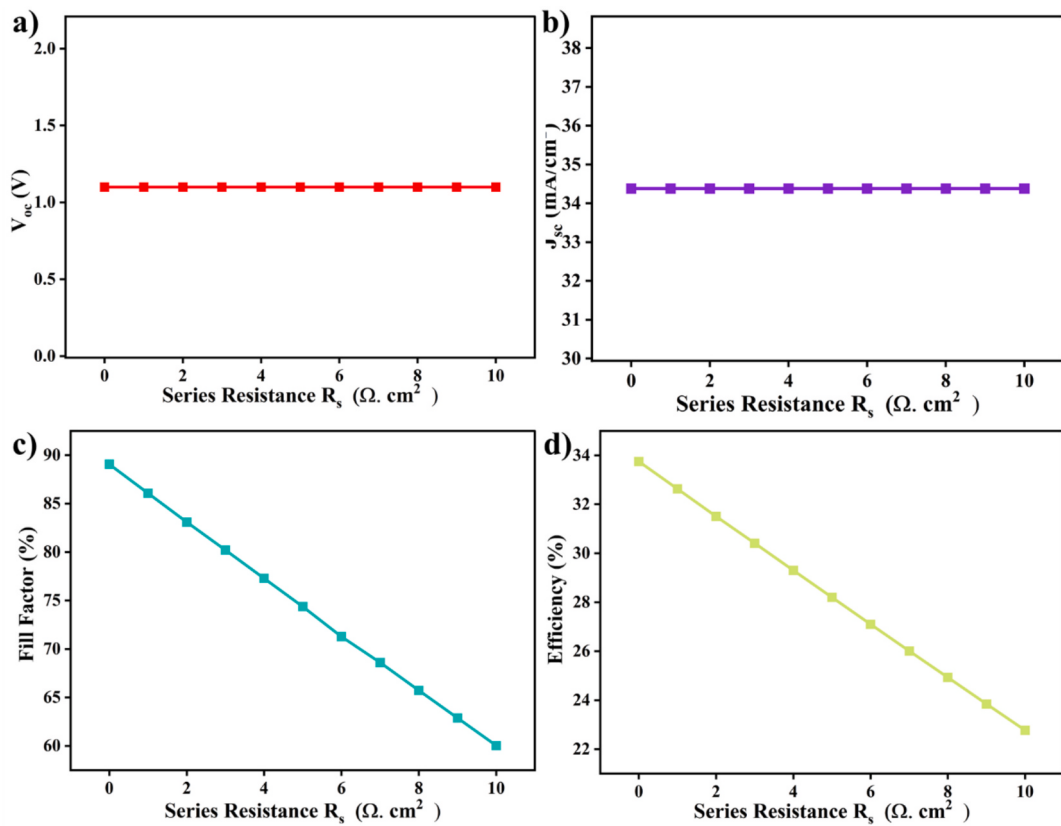


Fig. 15. Impact of R_s on the photovoltaic parameters of tan-PSCs: a) V_{oc} (V), b) J_{sc} (mA/cm 2), c) Fill factor (%), d) PCE (%).

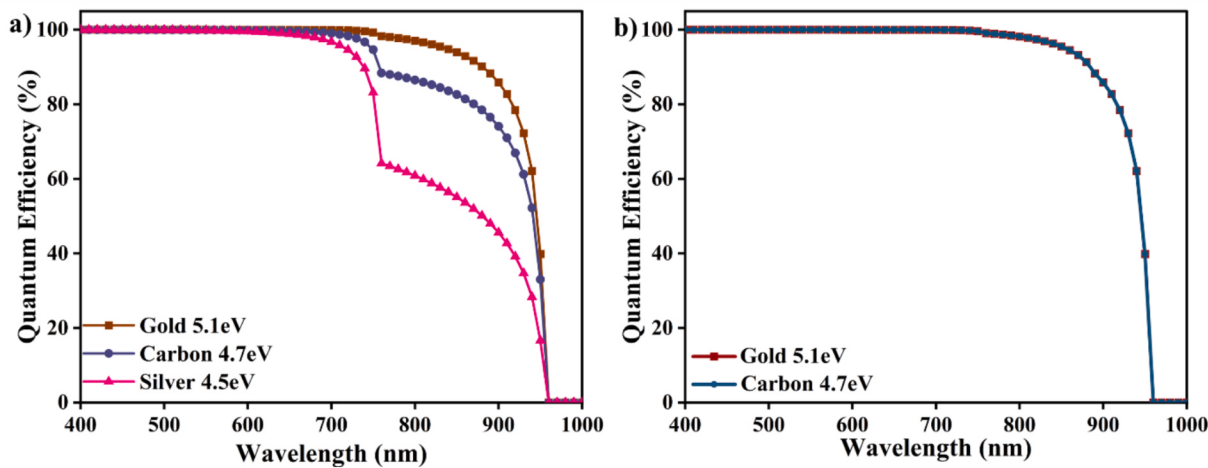


Fig. 16. Quantum efficiency (QE) spectra of tan-PSC with different back contacts, a) without CZTS, b) with CZTS.

This stability suggests that the $\text{TiO}_2/\text{CsPbI}_3$ interface is inherently defect-tolerant within this range presumably due to the effective matching of energy levels and a sufficient built-in electric field for charge separation. However, beyond $1 \times 10^{16} \text{ cm}^{-2}$, Fig. 13 reveals a noticeable drop in performance. At $1 \times 10^{18} \text{ cm}^{-2}$, the V_{oc} decreases to 0.90 V, and the PCE falls to 20.33 %, reflecting increased trap-assisted non-radiative recombination at the interface.

3.2.4. Effect of $\text{CsPbI}_3/\text{CsSnI}_3$ interfacial DD

The impact of interface DD at the $\text{CsPbI}_3/\text{CsSnI}_3$ junction on the photovoltaic performance of tan-PSC was systematically evaluated by varying the interfacial defect density from 1×10^{10} to $1 \times 10^{18} \text{ cm}^{-2}$.

The results reveal a strong dependence of device performance on the interfacial quality, as summarized in Fig. 14 (a-d). At a low DD of $1 \times 10^{10} \text{ cm}^{-2}$, the device achieves excellent performance with a V_{oc} of 0.96 V, J_{sc} of 34.38 mA/cm 2 , fill factor of 79.79 %, and a PCE of 26.45 %, indicating efficient charge transfer across the interface with minimal recombination. As the interface defect density increases, a significant deterioration in V_{oc} , FF, and ultimately PCE is observed. At $1 \times 10^{13} \text{ cm}^{-2}$, the V_{oc} drops to 0.60 V, and the PCE falls to 15.59 %, highlighting enhanced non-radiative recombination due to trap states formed at the interface. By $1 \times 10^{16} \text{ cm}^{-2}$, the PCE is further reduced to 8.00 %, driven by severe carrier recombination and a sharp decrease in J_{sc} to 27.28 mA/cm 2 . These findings indicate that interface trap states

Table 4

Simulated performance of tan-PSCs using SCAPS-1D, highlighting improvements over previous reports.

Device configuration	V _{oc} (V)	J _{sc} (mA/cm ²)	FF (%)	PCE (%)	Reference
FTO/TiO ₂ /CsGeI ₂ Br/CsGeI ₃ /P3HT/Au	1.2268	32.79	79.19	31.86	[23]
FTO/ZnO/CsPbI ₂ Br/CsPbI ₂ Br/CuSCN/Au	1.55	15.94	83.24	20.62	[41]
FTO/ZnO/CsPbI ₃ /CsPbBr ₃ /CuSCN/Carbon	1.40	19.77	84.86	23.59	[42]
ITO/ZnSe/CsBi ₃ I ₁₀ /GaAs/NiO/Au	1.03	30.2	88.1	27.40	[43]
FTO/ZnO/Cs ₂ TiCl ₆ /Cs ₂ TiI ₆ /Cs ₂ TiBr ₆ /NiO/Pt	1.35	24.70	82	27.36	[44]
ITO/ZnSe/CsPbI ₃ /CsSnI ₃ /Au	2.245	14.673	89.20	29.38	[45]
FTO/TiO ₂ /CsPbI ₃ /CsSnI ₃ /Au	1.10	34.38	89.06	33.79	This work

between CsPbI₃ and CsSnI₃ significantly impact the charge carrier dynamics, reducing separation of quasi-Fermi levels and hindering efficient carrier extraction.

3.2.5. Influence of series resistance

The effect of series resistance (R_s) on the photovoltaic performance of tan-PSCs is illustrated in Fig. 15(a-d), varying R_s from 0 to 10 Ω.cm², with the corresponding results highlighting its critical influence on charge transport. As R_s increases, the J_{sc} and V_{oc} remain constant (34.38 mA/cm² and 1.10 V, respectively), indicating unaffected photogeneration. However, the FF and PCE decline sharply, from 89.06 % and 33.75 % at 0 Ω.cm² to 60.04 % and 22.77 % at 10 Ω.cm², respectively. Increased series resistance introduces ohmic losses along the carrier transport pathway, especially at interfaces and grain boundaries, where misaligned energy levels and localised defect states impede carrier flow. This additional resistance causes voltage drops across the device under operating conditions, reducing the peak power delivery and lowering the Fill Factor. Moreover, higher R_s leads to inefficient extraction of photogenerated carriers, increasing the recombination probability.

3.2.6. Quantum efficiency (QE) analysis of tandem PSC

The QE spectra of tan-PSCs with different back contacts, gold (5.1 eV), carbon (4.7 eV), and silver (4.5 eV), are presented in Fig. 16, comparing device response without and with the CZTS interlayer. In the absence of CZTS, the QE notably varies with back contact selection. Gold exhibits a superior spectral response across the 400–950 nm range, attributed to its favorable work function alignment with the VBM of the perovskite (CsSnI₃) layer, minimising energy barriers for hole extraction. In contrast, carbon and silver contacts induce interfacial energy mismatches, leading to elevated carrier accumulation, non-radiative recombination at the CsSnI₃ interface, and reduced carrier collection, especially evident in the steep QE drop beyond 750 nm for silver. The presence of interface traps and poor orbital overlap at the CsSnI₃/contact interface results in enhanced trap-assisted recombination and localised energetic disorder. However, after the inclusion of CZTS as a hole transport interlayer, the QE spectra for gold and carbon become nearly indistinguishable and close to 100 % across the entire visible spectrum. This is due to the band alignment and defect passivation offered by CZTS, which bridges the energy level mismatch between CsSnI₃ and the back contact. The improved band bending and interfacial orbital continuity significantly enhance charge extraction and suppress recombination losses. This confirms that interlayer engineering can enable cost-effective electrodes like carbon to rival gold, offering a pathway toward scalable and high-efficiency tan-PSCs.

3.2.7. Performance Comparison of tan-PSCs based on SCAPS-1D simulations

Table 4 presents a comparative analysis of simulated performance for various tan-PSC architectures using SCAPS-1D. The current work distinguishes itself by achieving a remarkable PCE of 33.79 % with a simplified and fully inorganic device structure (FTO/TiO₂/CsPbI₃/CsSnI₃/Au). Unlike many previous designs that rely on multiple electron and hole transport layers—often including organic—this architecture employs a single electron transport layer (TiO₂) across both subcells and eliminates the use of organic hole transport materials. Additionally, this study is among the first to showcase the capabilities of lead-tin mixed halide perovskite tandems, showing that a carefully optimized bandgap-graded configuration using CsPbI₃ and CsSnI₃ can outperform traditional Pb-Pb tandems. These innovations not only simplify fabrication but also highlight the promise of all-inorganic tandem PSC for achieving excellent performance with improved durability and scalability.

4. Conclusion

This study demonstrates the high potential of a fully inorganic perovskite–perovskite tandem-inspired solar cell architecture employing a CsPbI₃/CsSnI₃ heterojunction. The optimised HTL-free configuration not only achieved an impressive power conversion efficiency of 33.75 %, surpassing the HTL-based counterpart, but also underscores the effectiveness of energy level alignment and charge transport within the all-inorganic framework. The successful integration of cost-effective carbon contacts and CZTS buffer layers further supports the viability of replacing conventional noble metals and organic transport materials without sacrificing performance. These findings affirm that simplified and scalable perovskite solar cells can be realised through strategic material and interface engineering, paving the way for next-generation photovoltaic technologies with enhanced environmental and economic sustainability.

CRediT authorship contribution statement

Jothika Balasubramaniyan: Writing – original draft, Formal analysis, Data curation, Conceptualization. **Thangaraji Vasudevan:** Methodology, Investigation, Formal analysis, Conceptualization. **Govindaraj Rajamanickam:** Supervision, Methodology, Investigation, Conceptualization. **Lung-Chien Chen:** Writing – review & editing, Supervision, Resources, Methodology.

Declaration of Competing Interest

The authors declare that they have no known competing financial interests or personal relationships that could have appeared to influence the work reported in this paper.

Acknowledgement

This research was supported by the Ministry of Science and Technology (MOST), Taiwan (Contract No. 111-2221-E-027-040-MY3), and the National Taipei University of Technology-Industry Joint Research Program, Taiwan (Contract No. 211A171).

References

- [1] A.M. Mitrašinović, Photovoltaics advancements for transition from renewable to clean energy, Energy 237 (2021) 121510, <https://doi.org/10.1016/j.energy.2021.121510>.
- [2] R. Sharma, A. Sharma, S. Agarwal, M.S. Dhaka, Stability and efficiency issues, solutions and advancements in perovskite solar cells: a review, Sol. Energy 244 (2022) 516–535, <https://doi.org/10.1016/j.solener.2022.08.001>.
- [3] P. Roy, N. Kumar Sinha, S. Tiwari, A. Khare, A review on perovskite solar cells: Evolution of architecture, fabrication techniques, commercialization issues and status, Solar Energy 198 (2020) 665–688, <https://doi.org/10.1016/j.solener.2020.01.080>.

- [4] J. Qian, B. Xu, W. Tian, A comprehensive theoretical study of halide perovskites ABX₃, *Org. Electron.* 37 (2016) 61–73, <https://doi.org/10.1016/j.orgel.2016.05.046>.
- [5] L. Qiu, S. He, L.K. Ono, Y. Qi, Progress of Surface Science Studies on ABX₃-based Metal Halide Perovskite Solar Cells, *Adv. Energy Mater.* 10 (2020) 1902726, <https://doi.org/10.1002/aenm.201902726>.
- [6] Y. Shi, J.J. Berry, F. Zhang, Perovskite/Silicon Tandem Solar Cells: Insights and Outlooks, *ACS Energy Lett.* 9 (2024) 1305–1330, <https://doi.org/10.1021/acsenergylett.4c00172>.
- [7] A. Urbina, The balance between efficiency, stability, and environmental impacts in perovskite solar cells: a review, *J. Phys. Energy* 2 (2020) 022001, <https://doi.org/10.1088/2515-7655/ab5ee>.
- [8] A. Machin, F. Márquez, Advancements in Photovoltaic Cell Materials: Silicon, Organic, and Perovskite Solar Cells, *Materials* 17 (2024) 1165, <https://doi.org/10.3390/ma17051165>.
- [9] F. Li, M. Liu, Recent efficient strategies for improving the moisture stability of perovskite solar cells, *J. Mater. Chem. A* 5 (2017) 15447–15459, <https://doi.org/10.1039/C7TA01325F>.
- [10] L.C. Palilis, M. Vasilopoulou, A. Verykios, A. Soultati, E. Polydorou, P. Argitis, D. Davazoglou, R. Abd Bin Mohd Yusoff, M.K. Nazeeruddin, Inorganic and Hybrid Interfacial Materials for Organic and Perovskite Solar Cells, *Adv. Energy Mater.* 10 (2020) 2000910, <https://doi.org/10.1002/aenm.202000910>.
- [11] W. Yan, Y. Sun, X. Zhao, W. Yang, B. Li, D. Zhong, F. Lu, W.-H. Wang, Carrier mobilities and band alignments of inorganic perovskites CsBx 3, *J. Mater. Chem. C* 12 (2024) 10733–10741, <https://doi.org/10.1039/D4TC01939C>.
- [12] E. Akman, T. Ozturk, W. Xiang, F. Sadegh, D. Prochowicz, M. Mahdi Tavakoli, P. Yadav, M. Yilmaz, S. Akin, The effect of B-site doping in all-inorganic CsPbI_xBr_{3-x} absorbers on the performance and stability of perovskite photovoltaics, *Energ. Environ. Sci.* 16 (2023) 372–403, <https://doi.org/10.1039/D2EE01070D>.
- [13] F. Bella, P. Renzi, C. Cavallo, C. Gerbaldi, Caesium for Perovskite Solar Cells: an Overview, *Chemistry – a European Journal* 24 (2018) 12183–12205, <https://doi.org/10.1002/chem.201801096>.
- [14] C. Ming, H. Zhou, J. Wu, C. Hu, W. Fan, X. Ma, Z. Zeng, Y. Qi, J. Shi, S. Qiao, The design and performance optimization of all-inorganic CsPbBr₂/CsSnI₃ heterojunction perovskite solar cells, *Sol. Energy* 263 (2023) 111885, <https://doi.org/10.1016/j.solener.2023.111885>.
- [15] Z. Yao, W. Zhao, Shengzhong (Frank) Liu, Stability of the CsPbI₃ perovskite: from fundamentals to improvements, *J. Mater. Chem. A* 9 (2021) 11124–11144, <https://doi.org/10.1039/DITA01252E>.
- [16] H. Yuan, Y. Zhao, J. Duan, Y. Wang, X. Yang, Q. Tang, All-inorganic CsPbBr₃ perovskite solar cell with 10.26% efficiency by spectra engineering, *J. Mater. Chem. A* 6 (2018) 24324–24329, <https://doi.org/10.1039/C8TA08900K>.
- [17] S. Ullah, F. Khan, J.F. Rasheed, Prospects for Commercialization of CsPbI₂-Based All-Inorganic Perovskite Solar Cells: Fabrication, Stability, and Engineering Strategies, *Advanced Functional Materials* n/a (n.d.) 2503508. <https://doi.org/10.1002/adfm.202503508>.
- [18] M. Ikram, R. Malik, R. Raees, M. Imran, F. Wang, S. Ali, M. Khan, Q. Khan, M. Maqbool, Recent advancements and future insight of lead-free non-toxic perovskite solar cells for sustainable and clean energy production: a review, *Sustainable Energy Technol. Assess.* 53 (2022) 102433, <https://doi.org/10.1016/j.seta.2022.102433>.
- [19] J. Borah, S. Baruah, S. Rajasekaran, Device Engineering of a Novel Lead-Free Solar Cell Architecture Utilizing Inorganic CsSnCl₃ and CsSnI₃ Perovskite-based dual Absorbers for Sustainable Powering of Wireless Networks, *J. Electron. Mater.* 54 (2025) 944–961, <https://doi.org/10.1007/s11664-024-11605-9>.
- [20] H. Wang, H. Li, W. Cai, P. Zhang, S. Cao, Z. Chen, Z. Zang, Challenges and strategies relating to device function layers and their integration toward high-performance inorganic perovskite solar cells, *Nanoscale* 12 (2020) 14369–14404, <https://doi.org/10.1039/DONR03408H>.
- [21] M. Khalid Hossain, G.F. Ishraque Toki, I. Alam, R. Pandey, D.P. Samajdar, M. Ferdous Rahman, M. Rasidul Islam, M.H.K. Rubel, H. Bencherif, J. Madan, M.K. A. Mohammed, Numerical simulation and optimization of a CsPbI₃-based perovskite solar cell to enhance the power conversion efficiency, *New J. Chem.* 47 (2023) 4801–4817, <https://doi.org/10.1039/D2NJ06206B>.
- [22] A. Saidarsan, S. Guruprasad, A. Malik, P. Basumatary, D.S. Ghosh, A critical review of unrealistic results in SCAPS-1D simulations: Causes, practical solutions and roadmap ahead, *Sol. Energy Mater. Sol. Cells* 279 (2025) 113230, <https://doi.org/10.1016/j.solmat.2024.113230>.
- [23] A.D.K. Kenfack, N.M. Thantscha, M. Msimanga, Simulation of Lead-Free Heterojunction CsGeI₂Br_x/CsGeI₃-based Perovskite Solar Cell using SCAPS-1D, *Solar* 3 (2023) 458–472, <https://doi.org/10.3390/solar3030025>.
- [24] S. Karthick, S. Velumani, J. Bouclé, Experimental and SCAPS simulated formamidinium perovskite solar cells: a comparison of device performance, *Sol. Energy* 205 (2020) 349–357, <https://doi.org/10.1016/j.solener.2020.05.041>.
- [25] A. Husainat, W. Ali, P. Cofie, J. Attia, J. Fuller, Simulation and Analysis of Methylammonium Lead Iodide (CH₃ NH₃)₂PbI₄ Perovskite Solar Cell with Au contact using SCAPS 1D Simulator, *AJOP* 7 (2019) 33. <https://doi.org/10.11648/j.ajop.20190702.12>.
- [26] M.K. Hossain, M.K.A. Mohammed, R. Pandey, A.A. Arnab, M.H.K. Rubel, K. M. Hossain, M.H. Ali, M.F. Rahman, H. Bencherif, J. Madan, M.R. Islam, D. P. Samajdar, S. Bhattacharai, Numerical Analysis in DFT and SCAPS-1D on the Influence of different Charge Transport Layers of CsPbBr₃ Perovskite Solar Cells, *Energy Fuels* 37 (2023) 6078–6098, <https://doi.org/10.1021/acs.energyfuels.3c00035>.
- [27] A. Zhang, R. Duan, Design and Numerical Investigation of CsPbI₃/CsSnI₃ Double-Absorption-Layer Heterojunction Perovskite Solar Cells Based on SCAPS-1D, *Physica Status Solidi (a)* 220 (2023) 2300525. <https://doi.org/10.1002/pssa.202300525>.
- [28] M.K. Hossain, M.H.K. Rubel, G.F.I. Toki, I. Alam, M.F. Rahman, H. Bencherif, Effect of Various Electron and Hole Transport Layers on the Performance of CsPbI₃-based Perovskite Solar Cells: a Numerical Investigation in DFT, SCAPS-1D, and wxAMPS Frameworks, *ACS Omega* 7 (2022) 43210–43230, <https://doi.org/10.1021/acsomega.2c05912>.
- [29] H.-J. Park, H. Son, B.-S. Jeong, SCAPS-1D simulation for Device Optimization to Improve Efficiency in Lead-Free CsSnI₃ Perovskite Solar Cells, *Inorganics* 12 (2024) 123, <https://doi.org/10.3390/inorganics12040123>.
- [30] K.B. Chavan, S.V. Desarada, S. Chaire, N.B. Chaure, Dark current in FTO/CZTS interface: a comprehensive comparison of practical Vs theoretical approach using SCAPS-1D, *Phys. Scr.* 99 (2024) 115947, <https://doi.org/10.1088/1402-4896/ad7b82>.
- [31] P. Liu, Q. Sun, F. Zhu, K. Liu, K. Jiang, L. Liu, Q. Li, S. Fan, Measuring the Work Function of Carbon Nanotubes with Thermionic Method, *Nano Lett.* 8 (2008) 647–651, <https://doi.org/10.1021/nl0730817>.
- [32] M. Minbashi, A. Ghobadi, M.H. Ehsani, H. Rezagholipour Dizaji, N. Memarian, Simulation of high efficiency SnS-based solar cells with SCAPS, *Solar Energy* 176 (2018) 520–525, <https://doi.org/10.1016/j.solener.2018.10.058>.
- [33] M. Aliaghayee, Optimization of the Perovskite Solar Cell Design with Layer Thickness Engineering for improving the Photovoltaic Response using SCAPS-1D, *J. Electron. Mater.* 52 (2023) 2475–2491, <https://doi.org/10.1007/s11664-022-10203-x>.
- [34] P. Srivastava, S. Sadanand, P. Rai, D.K. Lohia, H. Dwivedi, A. Qasem, S. Umar, H. Akbar, S.B. Algadi, Theoretical study of perovskite solar cell for enhancement of device performance using SCAPS-1D, *Phys. Scr.* 97 (2022) 125004, <https://doi.org/10.1088/1402-4896/ac9dc5>.
- [35] S. Marimuthu, S. Shriswaroop, M. Muthumareeswaran, S. Pandiaraj, A. N. Alodhayb, T.A. Alrebedi, A. Nirmala Grace, Drift diffusion modelling of cell parameters effect on the performance of perovskite solar cells with MXene as additives, *Solar Energy* 262 (2023) 111804, <https://doi.org/10.1016/j.solener.2023.111804>.
- [36] S. Rabhi, K. Sekar, K. Kalna, Y.I. Bouderbala, N. Bouri, N. Oueldina, N. Belbachir, K. Dadda, M.S. Aida, N. Attaf, Experimental findings and SCAPS-1D simulations for high-efficiency MAPbI₃ perovskite solar cells beyond 31%, *Opt. Quant. Electron.* 56 (2024) 1372, <https://doi.org/10.1007/s11082-024-07282-x>.
- [37] F. Saeed, M. Haseeb Khan, H.A. Tauqueer, A. Haroon, A. Idrees, S.M. Shehrazi, L. Prokop, V. Blazek, S. Misak, N. Ullah, Numerical Investigation of Photo-Generated Carrier Recombination Dynamics on the Device Characteristics for the Perovskite/Carbon Nitride Absorber-Layer Solar Cell, *Nanomaterials* 12 (2022) 4012, <https://doi.org/10.3390/nano12224012>.
- [38] S. Yasin, T. Al Zoubi, M. Moustafa, Design and simulation of high efficiency lead-free heterostructure perovskite solar cell using SCAPS-1D, *Optik* 229 (2021) 166258, <https://doi.org/10.1016/j.ijleo.2021.166258>.
- [39] P.T. Webster, R.A. Carrasco, A.T. Newell, J.V. Logan, P.C. Grant, D. Maestas, C. P. Morath, Utility of Shockley–Read–Hall analysis to extract defect properties from semiconductor minority carrier lifetime data, *J. Appl. Phys.* 133 (2023) 125704, <https://doi.org/10.1063/5.0147482>.
- [40] S.H. Zyoud, A.H. Zyoud, N.M. Ahmed, A.R. Prasad, S.N. Khan, A.F.I. Abdelkader, M. Shahwan, Numerical Modeling of High Conversion Efficiency FTO/ZnO/CdS/CZTS/MO Thin Film-based Solar Cells: using SCAPS-1D Software, *Crystals* 11 (2021) 1468, <https://doi.org/10.3390/cryst11121468>.
- [41] S. Khatoon, V. Chakraborty, S.K. Yadav, S. Diwakar, J. Singh, R.B. Singh, Simulation study of CsPbIxBr_{1-x} and MAPbI₃ heterojunction solar cell using SCAPS-1D, *Sol. Energy* 254 (2023) 137–157, <https://doi.org/10.1016/j.solener.2023.02.059>.
- [42] P. Debnath, J. Sarkar, A. Talukdar, S. Chatterjee, Exploring the potential of CsPbI₃/CsPbBr₃ heterojunction as an absorber layer in perovskite solar cells: a numerical and experimental study, *Bull. Mater. Sci.* 47 (2024) 162, <https://doi.org/10.1007/s10204-024-03224-1>.
- [43] R. Khan, N. Farjana, J. Mst, J.Y. Akter Jim, M.R. Al-Humaidi, M.M.R. Islam, Numerical simulation and performance enhancement of CsBi₃I₁₀-based heterojunction solar cell with various semiconductor layers (CZTS, CZTGS, Al_{0.8}Ga_{0.2}Sb, GaAs) along with machine learning-based analysis, *Solar Energy* 295 (2025) 113539, <https://doi.org/10.1016/j.solener.2025.113539>.
- [44] M.A. Islam, R. Paul, A Lead-Free Inorganic Cs₂TiX₆-based Heterostructure Perovskite Solar Cell Design and Performance Evaluation, *Opt. Quantum Electron.* 55 (11) (2023) 957.
- [45] M.A. Oufakir, R.T. Alqahtani, Y. Chrifi, A. Ajbar, Next-gen solar: revealing the promise of CsPbI₃/CsSnI₃ tandem cells, *Solar Energy* 298 (2025) 113665, <https://doi.org/10.1016/j.solener.2025.113665>.